Atmos. Chem. Phys. Discuss., 13, 1489–1526, 2013
www.atmos-chem-phys-discuss.net/13/1489/2013/
doi:10.5194/acpd-13-1489-2013

Atmospheric Chemistry and Physics Discussions

Modeling microphysical effects of entrainment in clouds observed during EUCAARI-IMPACT field campaign

D. Jarecka[1], **H. Pawlowska**[1], **W. W. Grabowski**[2], **and A. A. Wyszogrodzki**[2]

[1]Institute of Geophysics, Faculty of Physics, University of Warsaw, Warsaw, Poland
[2]National Center for Atmospheric Research, Boulder, Colorado, USA

Received: 13 December 2012 – Accepted: 21 December 2012 – Published: 15 January 2013

Correspondence to: D. Jarecka (dorota@igf.fuw.edu.pl)

Published by Copernicus Publications on behalf of the European Geosciences Union.

Abstract

This paper discusses aircraft observations and large-eddy simulation (LES) of the 15 May 2008, North Sea boundary-layer clouds from the EUCAARI-IMPACT field campaign. These clouds were advected from the north-east by the prevailing lower-tropspheric winds, and featured stratocumulus-over-cumulus cloud formations. Almost-solid stratocumulus deck in the upper part of the relatively deep weakly decoupled marine boundary layer overlaid a field of small cumuli with a cloud fraction of $\sim 10\,\%$. The two cloud formations featured distinct microphysical characteristics that were in general agreement with numerous past observations of strongly-diluted shallow cumuli on the one hand and solid marine boundary-layer stratocumulus on the other. Macrophysical and microphysical cloud properties were reproduced well by the double-moment warm-rain microphysics large-eddy simulation.

A novel feature of the model is its capability to locally predict homogeneity of the subgrid-scale mixing between the cloud and its cloud-free environment. In the double-moment warm-rain microphysics scheme, the homogeneity is controlled by a single parameter α, that ranges from 0 to 1 and limiting values representing the homogeneous and the extremely inhomogeneous mixing scenarios, respectively. Parameter α depends on the characteristic time scales of the droplet evaporation and of the turbulent homogenization. In the model, these scales are derived locally based on the subgrid-scale turbulent kinetic energy, spatial scale of cloudy filaments, the mean cloud droplet radius, and the humidity of the cloud-free air entrained into the cloud. Simulated mixing is on average quite inhomogeneous, with the mean parameter α around 0.7 across the entire depth of the cloud field, but with local variations across almost the entire range, especially near the base and the top of the cloud field.

ACPD

13, 1489–1526, 2013

1 Introduction

Numerical simulation of cloud microphysical properties poses significant challenges. This is because of the range of spatial scales involved, from the scale of a cloud or cloud system (hundreds of meters to tens or hundreds of kilometers) down to sub-centimeter scales at which cloud microphysical processes operate. Resolving such a range of scales in a numerical model is yet not possible. Cloud-scale dynamics (with help from even larger-scale processes) determine overall cloud characteristics, such as the cloud depth, horizontal extent, lifetime, etc. It also provides energy for smaller-scale turbulent motions, for instance, through the instabilities of the cloud-environment interface (Grabowski and Clark, 1991, 1993a,b). Resolving cloud-scale dynamics requires model gridlengths ranging from tens of meters to a kilometer or so depending on the particular case. Processes operating at smaller scales can only be included through the subgrid-scale modeling. This especially applies to cloud entrainment where dry environmental air is brought into the cloud and affects cloud macro- and microphysical characteristics. Entrainment is typically driven by interface instabilities, especially in the case of cumulus clouds, but it may be also affected by other processes, for instance, by the buoyancy reversal due to cloud evaporation (see Kuo and Schubert, 1988; Siems et al., 1990; Grabowski, 1993, 1995). Details of how entrainment affects cloud microphysics are still poorly understood because of difficulties encountered in cloud observations (mostly because of the aircraft speed and response time of aircraft cloud probes) and the limited range of spatial scales resolved in numerical modeling.

Entrainment and mixing typically lead to a reduction of the cloud liquid water content (LWC), but microphysical effects can vary widely. In the homogeneous mixing, the dilution leads to the reduction of the droplet size, with a decrease of droplet concentration only due to changes of the total cloudy volume. When the extremely inhomogeneous mixing takes place, droplet concentration is reduced without effects on the droplet radius. Both droplet radius and concentration are reduced in the intermediate case of the inhomogeneous mixing. The homogeneity of mixing has been argued to depend on the

ACPD
13, 1489–1526, 2013

relative magnitude of the time scales for droplet evaporation and for turbulent homogenization (Baker and Latham, 1979; Baker et al., 1980; Jensen and Baker, 1989; Burnet and Brenguier, 2007; Andrejczuk et al., 2009; Lehmann et al., 2009). Homogeneous mixing takes place when the turbulent homogenization time scale is much smaller than the droplet evaporation time scale because only then all droplets are exposed to the same conditions during evaporation. In the opposite limit, when the turbulent homogenization time scale is much larger than the droplet evaporation time scale, extremely inhomogeneous mixing is thought to occur. In such a limit, some droplets evaporate completely and the rest does not experience any evaporation at all.

In contrast to what is implicitly assumed in cloud models, the homogenization of a gridbox experiencing turbulent mixing does not take place instantaneously, but is associated with possibly a significant delay due to turbulent stirring. During the stirring, an initially coarsely mixed and partially cloudy volume gradually evolves towards microscale homogenization (see discussion in Grabowski, 2007). Arguably, early stages of the turbulent stirring are associated with the extremely inhomogeneous mixing because only droplets near filament edges evaporate completely (i.e. the mean droplet concentration is reduced without changing the mean droplet size). As the stirring progresses, scales of cloudy filaments decrease and eventually approach the scale of microscale homogenization, that is, the Kolmogorov microscale. At this stage, all droplets are exposed to the same subsaturation and mixing approaches the homogeneous limit. Modeling of such a chain of events requires special subgrid-scale turbulent stirring scheme, for instance, as proposed in Grabowski (2007) and further developed in Jarecka et al. (2009). Jarecka et al. (2013, hereinafter JGMP13) merged the delayed evaporation (stirring) scheme with the double-moment bulk warm-rain microphysics scheme to allow prediction of the local mixing scenario. Herein, we apply the large-eddy simulation model equipped with the subgrid scale stirring/evaporation scheme of JGPM13 to the cloud case observed during the EUCAARI-IMPACT field project.

The next section briefly describes the specific case from the EUCAARI-IMPACT campaign selected for the modeling study. Section 3 provides details of the LES model and

ACPD
13, 1489–1526, 2013

modeling setup. Model results are compared to observations in Sect. 4, and simulated mixing characteristics are analyzed in Sect. 5. Conclusions are presented in Sect. 6.

2 The EUCAARI-IMPACT field campaign and the 15 May 2008, North Sea case

The EUCAARI-IMPACT (Intensive Observation Period At Cabauw Tower) field campaign was part of the EUCAARI (European Integrated Project on Aerosol Cloud Climate and Air Quality Interactions, Kulmala et al., 2011) project funded under the EU Framework Programme 6. The campaign took place in May 2008 in the Netherlands and focused on remote sensing and in-situ ground-based and airborne observations of clouds and aerosols in the vicinity of the Cabauw tower. Because of unexpectedly dry and cloudless conditions that prevail over the Netherlands for most of the EUCAARI-IMPACT campaign, several scientific flights were conducted over the North Sea. These flights targeted clouds and aerosols within the stratocumulus-topped marine boundary layer. The 15 May flight was one of such cases (Puygrenier et al., 2010).

Figure 1 shows flight trajectory of the 15 May Meteo-France Safire ATR-42 mission superimposed on the MODIS satellite image at 11:15 UTC. The figure shows a significant cloud cover over the North Sea and the surrounding land masses. Shallow convective clouds over the eastern England, just to the west of the Greenwich meridian, document the low-level north-easterly flow over the region, in agreement with the aircraft data (see Fig. 2). The stratocumulus deck over the North Sea extends to the north of approximately the 54° N parallel and appears quite spatially heterogeneous. The stratocumulus topped boundary layer (STBL) and the lower free troposphere were sampled by the aircraft between approximately 07:40 and 09:30 UTC. Figure 2 shows the height of the aircraft as a function of time and depicts in red periods when the aircraft encountered a cloud. The figure shows that besides the stratocumulus cloud (with cloud base and cloud top around 700 and 1150 m), the aircraft often intersected clouds beneath the stratocumulus cloud base. Such a situation, often referred to as the boundary layer with stratocumulus over cumulus, corresponds to a weakly decoupled

ACPD
13, 1489–1526, 2013

relatively deep marine boundary layer, often associated with the transition from shallow STBL to significantly deeper cumulus-topped boundary layer in the subtropics (see Bretherton and Pincus, 1995; de Roode and Duynkerke, 1997; Sandu et al., 2010).

The cloud data from the flight track shown in Figs. 1 and 2 were divided into two sets depending on the height of the aircraft to represent the stratocumulus/cumulus clouds. The droplet concentration, cloud water mixing ratio, and mean volume radius for the two cloud types are shown in Figs. 3 and 4. Each data point in the figures represents approximately 100-m average (1-Hz) of cloud droplet counts from the FFSSP (Fast Forward Scattering Spectrometer Probe; Brenguier et al., 1998). The data corresponding to the stratocumulus cloud (Fig. 3) are shown as a function of height above the cloud base that varies between 650 m and 750 m. Figure 3 shows fairly typical pattern: approximately constant with height droplet concentration ($\sim 100\,\mathrm{mg}^{-1}$; except near the cloud base where FFSSP may miss small droplets and cloud top where intensive mixing takes place), cloud water mixing ratio not far from the adiabatic (but also with a significant spread, especially in the upper half of the cloud depth), and the mean volume radius increasing gradually with height and consistent with the observed concentrations. In contrast, the data for the cumuli (Fig. 4) show a wide range of droplet concentrations and relatively small values of the cloud water mixing ratio. The mean volume radius is small, in the range of 2 to 8 µm, that is, as in the lower part of the stratocumulus. All these suggest that small cumuli beneath stratocumulus are strongly diluted by entrainment and the 1-Hz data may not represent the small-scale features adequately. Because cumulus cloud fraction is low, there is a significantly lower number of data points in Fig. 4 compared to Fig. 3. Some of these cumuli are likely to penetrate into the stratocumulus layer; this may explain data points with cloud water exceeding the adiabatic value in Fig. 3b. These observations are compared to results of model simulations described in subsequent sections.

ACPD
13, 1489–1526, 2013

3 The numerical model, model setup, and model simulations

The model used in the simulations is the same as in JGMP13. The fluid flow model is the 3-D anelastic semi-Lagrangian/Eulerian model EULAG documented in Smolarkiewicz and Margolin (1997, model dynamics), Grabowski and Smolarkiewicz (1996, model thermodynamics), and Margolin et al. (1999, subgrid-scale turbulent mixing). Prusa et al. (2008) provide a recent review with comprehensive list of references. As in JGMP13, EULAG was setup as an LES model with the horizontal/vertical gridlength of 50/20 m and the computational domain of 6.4/3 km in horizontal/vertical direction. Periodic lateral boundary conditions were used, and free-slip rigid lid boundaries were assumed at the bottom and top boundaries. Model time step was 1 s. The model was run for 6 h, and snapshots of model fields saved every 3 min from the last 3 h of the simulation were used in the analysis.

Model thermodynamics combines the two-moment warm-rain scheme (i.e. predicting both the mixing ratio and the droplet concentration for the cloud and rain water; Morrison and Grabowski, 2007, 2008) with the delay of cloud water evaporation resulting from the subgrid-scale mixing between the cloud and its environment (Grabowski, 2007; Jarecka et al., 2009). Activation of cloud droplets is represented by the approach developed by Khvorostyanov and Curry (2006) with the total CCN concentration set to $200\,\mathrm{mg}^{-1}$. The latter is based on EUCAARI-IMPACT observations reported in Crumeyrolle et al. (2011). Autoconversion and accretion parameterization follow those proposed in Khairoutdinov and Kogan (2000) as used in Morrison and Grabowski (2007). The delay of cloud water evaporation during turbulent mixing is facilitated by including two additional model variables, the characteristic scale (width) λ of cloud filaments and the fraction of a gridbox volume occupied by the cloudy air β. The scale λ is assumed to decrease during the stirring phase of the entrainment process from the scale of an initial engulfment Λ (assumed to be of the order of the model gridlength) down to the scale of microscale homogenization λ_0 (i.e. of the order of the Kolmogorov microscale; ~ 1 mm in atmospheric conditions). The evaporation of cloud water due to

ACPD
13, 1489–1526, 2013

subgrid-scale mixing depends on the scale λ, with virtually no evaporation when $\lambda \sim \Lambda$, and all evaporation when $\lambda \sim \lambda_0$ (see discussion in Grabowski, 2007).

In the double-moment scheme the homogeneity of mixing is controlled by the parameter α (Morrison and Grabowski, 2008). The parameter α is calculated locally based on the predicted turbulent kinetic energy, the scale of cloud filaments λ, mean cloud droplet radius, and the humidity of the cloud-free air entrained into the cloud. Results of direct numerical simulations of the interfacial cloudy and cloud-free air mixing reported in Andrejczuk et al. (2009) are used in the prediction of α. See Appendix A and JGMP13 for more details.

The entire thermodynamics/microphysics scheme operates in the following way. For a gridbox with either $\lambda = \Lambda$ or $\lambda = 0$, that is, either fully cloudy or cloud-free, respectively, calculations progress as in the standard double-moment scheme of Morrison and Grabowski (2007, 2008) without any subgrid-scale considerations. For a gridbox with $\lambda_0 < \lambda < \Lambda$, the expected evaporation or condensation of cloud water δq_c is calculated first using the grid-averaged fields as in the standard double-moment scheme. If condensation is predicted, then the gridbox is assumed uniform, δq_c is applied in the microphysics scheme, λ is reset to Λ and β is reset to 1. The same procedure is used when $\lambda < \lambda_0$ because molecular homogenization is assumed completed. If needed, activation of new cloud droplets takes place. For the evaporation, δq_c is first partitioned into the adiabatic part $\beta C^{ad} \Delta t$ [where C^{ad} is the adiabatic condensation rate, see appendix in Grabowski (2007); and Δt is the model time step] and the contribution due to mixing Δq_c assuming $\Delta q_c = \delta q_c - \beta C^{ad} \Delta t$. Note that variable Δq_c, that is a part due to diabatic evaporation, combines impacts of the explicit (due to turbulent mixing terms) as well as the implicit (numerical) diffusion. Because of the delay of the diabatic evaporation during the stirring phase of the entrainment, only a fraction of Δq_c, $\Delta q_c^* = \lambda_0/\lambda \, \Delta q_c$ is allowed to evaporate. This formula comes from heuristic considerations concerning droplet evaporation at the edges of cloud filaments. Next, Δq_c^* is applied to the cloud water mixing ratio, and the droplet concentration is reduced depending on the homogeneity of the subgrid-scale mixing, that is, through the parameter α (see Appendix A).

ACPD
13, 1489–1526, 2013

In addition, the adiabatic condensation C^{ad} is applied to the β cloudy fraction of the gridbox assuming no change in the droplet concentration.

The idealization of observed mean conditions used to initialize the simulation are shown in Fig. 5. The total water mixing ratio, liquid water potential temperature and horizontal wind components are taken as $5.2\,g\,kg^{-1}$, 282.2 K, −3.18 and $-3.89\,m\,s^{-1}$ (E–W and N–S) up to the base of the STBL inversion at 1120 m. The inversion is assumed to be 40 m deep, with the profiles linearly changing to $3.1\,g\,kg^{-1}$, 289.6 K, −3.87 and $-0.98\,m\,s^{-1}$ at 1160 m. Above, the liquid water potential temperature (equal to the potential temperature in the absence of cloud condensate) increases linearly to 305.6 K at 3 km (i.e. the model top), whereas all other fields are assumed constant with values as at the inversion top.

The model is forced to maintain approximately steady-state conditions throughout the simulation, similarly to other LES boundary layer studies (e.g. Siebesma et al., 2003; Stevens et al., 2005). Forcings required to maintain approximately steady-state conditions are estimated by a trial and error test simulations. The forcings include: (a) surface heat and momentum fluxes; (b) large-scale subsidence; and (c) radiative processes. Surface heat fluxes and subsidence were assumed to be constant in time and space. Surface sensible and latent heat fluxes were derived by applying an estimate of the sea surface temperature (SST) from satellite analysis for this day. After some tests, the values were selected as constant $8\times10^{-3}\,K\,m\,s^{-1}$ for the sensible heat flux and $6.5\times10^{-5}\,m\,s^{-1}$ for the latent heat flux. The surface momentum fluxes were calculated similarly to Siebesma et al. (2003), with the fluxes given by $-u_*^2\mathbf{v}/|\mathbf{v}|$, with $u_* = 0.28\,m\,s^{-1}$. Large-scale subsidence was prescribed as $W_s = -Dz$ with the large-scale divergence selected as $D = 4\times10^{-6}\ s^{-1}$. For the radiative transfer, only the long-wave processes were considered as the key driver of the STBL dynamics and only in an extremely simplified way as proposed in Stevens et al. (2005, see Eqs. 3 and 4 there). The parameters in the simple approach were the same as in Stevens et al., except for the parameter controlling the cooling in the free atmosphere, α_z, which was taken as

ACPD
13, 1489–1526, 2013

half of the value given in Stevens et al. that is $\alpha_z = 0.5\,\mathrm{m}^{-4/3}$. Surface pressure was assumed to be 1015 hPa.

4 Model results: comparison with observations

Figure 6 shows evolution of selected bulk properties of the STBL for the entire length of the simulation, the liquid water path (LWP), the resolved kinetic energy (per unit of mass, E_{kin}), and the height of the inversion (z_{inv}, defined as the level of maximum potential temperature gradient). The figure illustrates the approximately steady-state conditions simulated by the model, with significant fluctuations of LWP (not atypical for such simulations; see Fig. 2 in Stevens et al., 2005), gradual decrease of the of E_{kin} and increase of z_{inv}. The figure shows that the simulation setup only approximately maintains the steady-state conditions.

To provide an illustration for the model results, Fig. 7 shows snapshots of the cloud water field in the two vertical cross sections of the computational domain at time of t = 6 h, i.e. at the end of the simulation. The figure also shows local values of the parameter α at points undergoing turbulent cloud-environment mixing. The figure shows that in the model, similarly as in the observations, the stratocumulus layer overlays a layer with shallow convective clouds that either grow into the stratocumulus layer (like the cloud near the center of the upper panel) or remain detached in the layer between 400 and 700 m (see the bottom panel). Such a situation is typical for relatively deep STBL and results from weak decoupling between the two cloud layers (see Bretherton and Pincus, 1995; de Roode and Duynkerke, 1997; Sandu et al., 2010). The figure also shows that mixing characteristics (i.e. the parameter α) vary significantly in various locations, from close to homogeneous ($\alpha = 0$, dark blue colors in the panels) to not far from extremely inhomogeneous ($\alpha = 1$, dark red colors).

The double-layer structure of clouds within STBL is also confirmed by the mean cloud fraction and in-cloud condensed water profiles shown in Fig. 8. To obtain these profiles, gridpoints of the model data were assumed cloudy if the cloud water mixing

ACPD
13, 1489–1526, 2013

ratio exceeded 0.01 g kg^{-1} and the droplet concentration exceeded 5 mg^{-1}. The cloud fraction within the cumulus layer is small ($\sim$ 0.1), but it is quite high, up to 0.9, within the stratocumulus layer. The cloud water shows that the cumulus layer (roughly between 300 and 700 m above the sea level) features clouds significantly diluted by entrainment, with the mean cloud water increasing with height at a rate lower than the adiabatic one (the latter is $\sim$ 1 g kg^{-1} per 500 m). The rate of increase within the lower part of the stratocumulus layer (between approximately 700 and 1000 m) is significantly higher. The reduction of the cloud water close to the cloud top comes from the cloud-top entrainment as illustrated by the number of gridpoints undergoing turbulent mixing (see colored points in Fig. 7).

Figure 9 shows the CFAD (contoured frequency by altitude diagram) of the cloud droplet concentration. The red line shows the average profile. Only cloudy grid points are included in the analysis and the cloud fraction profile is shown by the blue line on the right hand side of the panel. The figure shows that the two layers have different microphysical characteristics. The mean values inside the layers are approximately constant except close to the cloud top, cloud base and the transition layer between cumulus and stratocumulus. The mean concentration for the stratocumulus layer is around 90 mg^{-1}, and it is around 60 mg^{-1} for the cumulus layer. These are in a good agreement with observational values (see Figs. 4 and 3). The CFAD shows a large spread inside the cumulus layer, with the most frequent values around 20 mg^{-1} and some points with concentrations as high as 150 mg^{-1}. Because of the strongly skewed distribution, the mean and the most frequent values differ significantly. The distribution narrows within the stratocumulus layer, and the most frequent values are close to the mean. Similar features are present in the observations. The increase of the CFAD width near the top of the stratocumulus layer (i.e. above the level of 1100 m) likely comes from the mixing with the unsaturated air from above the cloud top.

Figure 10 shows the CFAD of β, the cloudy fraction of the gridbox volume. As expected, β is seldom different from unity in the stratocumulus layer, but vary widely within the cumulus layer and near the very stratocumulus top. It follows that predicted

ACPD
13, 1489–1526, 2013

gridbox-averaged droplet concentration N_c and the local droplet concentration N_c/β (i.e. the concentration in the cloudy part of volume) differ significantly in cumuli and near the stratocumulus top. These differences are consistent with the stirring phase of the cloud entrainment and mixing.

Figure 11 shows the CFAD of the droplet mean volume radius. The figure clearly shows that the two cloud layers are to a large extent decoupled. The most frequent values increase with height in both layers, and the separation between the layers is evident. The green lines show the adiabatic values of the radius assuming the cloud base height and the adiabatic droplet concentration of 300 m and 60 mg^{-1} for the cumulus layer, and 700 m and 90 mg^{-1} for the stratocumulus layer. In the stratocumulus layer, the most frequent values are close to the adiabatic profile. This indicates that the stratocumulus is only weakly diluted by entrainment, an aspect consistent with the observations (Fig. 3). For the cumulus layer, the most frequent values are much smaller than adiabatic, except near the cloud base, with radii smaller than 8 µm. Similar behavior is seen in the observations (see Fig. 4). This is again a consequence of strong dilution of cumulus clouds. Although some cumuli penetrate into the stratocumulus layer (see examples in Fig. 7) Fig. 11 clearly shows that this is not the dominant pattern.

5 Mixing scenarios

As explained in the previous section, the model predicts locally the mixing scenario at each time step by deriving the parameter α from model variables (see the Appendix A). Figure 7 shows local α values at grid volumes undergoing turbulent cloud-environment mixing. The figure shows that mixing events take place mostly at the edges of cumulus clouds and near the stratocumulus top. They occur less frequently inside the stratocumulus layer, typically at the edges of stratocumulus breaks (or holes) as one might expect (see discussion in Kurowski et al., 2009). Various colors refer to the values of the parameter α, documenting a large spread of their values.

ACPD
13, 1489–1526, 2013

Figure 12 shows CFAD of the parameter α for points undergoing turbulent mixing. The figure also shows the number of points (as a fraction of all points at a given level) included in the analysis. The figure shows that α changes from close to 0 (homogeneous mixing) to close to 1 (extremely inhomogeneous mixing) and the distribution is particularly wide near the bottom and top of the cloud layer. The red line shows the average profile. The profile is approximately constant across the cloud layer, except near the very bottom and very top. Although the cloud fraction in the cumulus layer is small, the mixing events occur often, approximately half of the cloudy points within the cumulus layer experience turbulent mixing. In the stratocumulus layer mixing events are rare, except near the cloud top. The most frequent mixing scenarios represent inhomogeneous mixing ($\alpha \approx 0.7$–0.8) across the most of the cloud layer depth (except of of the 100 m or so near the cloud base and cloud top). The width of the distribution is large, however, with α ranging from 0.3 to 0.9 throughout the most of the cloud field, with even wider range near the cloud base and cloud top. The differences between the two cloud layers seem rather small. This might be viewed surprising considering significant differences between cumulus and stratocumulus clouds, expected levels of turbulence, for instance (e.g. Siebesma et al., 2003; Stevens et al., 2005; Burnet and Brenguier, 2007). The analysis below further explores the similarity and differences.

Parameter α is a function of the characteristic time scales of the droplet evaporation, τ_{evap}, and of the turbulent mixing, τ_{mix}. The Appendix A presents formulas that are used to locally derive α from τ_{evap} and τ_{mix}, and the time scales from model variables. More in-depth discussion is provided in JGMP13.

CFADs of the time scale τ_{evap} and τ_{mix} are shown in Fig. 13. The figure shows that the two cloud layers differ more significantly in the time scales than in α. CFADs are wider within most of the stratocumulus layer when compared to the cumulus layer. The mixing time scale τ_{mix} is smaller in the cumulus layer. This is caused mostly by differences in TKE predicted by the model, which is higher in cumulus layer and close to the top of the stratocumulus. This agrees with previous modeling studies (Siebesma et al., 2003; Stevens et al., 2005). The evaporation time scale τ_{evap} is approximately the

ACPD
13, 1489–1526, 2013

same within the two layers (except near the cloud base and stratocumulus top where the distribution is particularly wide). This is consistent with the fact that droplet radii are similar in both layers (Fig. 11). Cumulus clouds are shallow and very diluted, so droplets cannot grow to large sizes. This is against a common assumption that cloud droplets within stratocumulus are smaller and thus evaporation is faster. The small values of the evaporation time scale near the stratocumulus top are due to lower humidities of the entrained air, as shown below.

Figures 14 and 15 show scatter diagrams of model variables (in appropriate powers, see the Appendix A) that determine the actual values of the τ_{evap} and τ_{mix} at the height of 500 m (i.e. within the cumulus layer) and 1200 m (i.e. near the stratocumulus top), respectively. There are systematic differences between Figs. 14 and 15, consistent with expected differences between entrainment in cumulus and stratocumulus. For instance, there are more points with higher TKE in the cumulus layer, as well as larger droplet sizes near the stratocumulus top (that was already pointed out in the previous analysis). The relative humidity RH_d of air involved in the subgrid-scale turbulent mixing is typically quite high (0.9 and above so that $1/(1 - RH_d)$ is larger than 10), but it is shifted towards lower humidities for the stratocumulus layer. This is consistent with the fact that stratocumulus entrains significantly drier air from above the inversion.

6 Conclusions

This paper presents aircraft observations and LES modeling of the 15 May 2008, boundary-layer clouds over the North Sea observed during the EUCAARI-IMPACT field campaign. These clouds were advected from the north-east by the prevailing lower tropspheric winds and were sampled by the aircraft between approximately 07:40 and 09:30 UTC. Almost-solid stratocumulus deck was present in the upper part of the relatively deep weakly decoupled marine boundary layer. Small cumuli, with a cloud fraction of ∼10 %, were sampled beneath the stratocumulus. The two cloud formations featured distinct microphysical characteristics. Small cumuli were significantly diluted

ACPD
13, 1489–1526, 2013

and featured low LWC, typically below 0.2 g kg^{-1}, droplet radii between 2 and 8 µm, and a wide rage of droplet concentrations, between a few to about 100 mg^{-1}. No systematic variation of these parameters with height was observed. Small-scale structure of these cumuli were unlikely resolved by the observations. In contrast, stratocumulus deck observations were consistent with results of previous studies of such clouds. Stratocumulus is only weakly diluted, droplet concentrations ranged between 50 and 150 mg^{-1} and were approximately height-independent (except near the cloud top where lower concentrations were observed). The mean droplet radius is observed to increase with height in a manner consistent with the close-to-adiabatic LWC and the mean droplet concentration.

To simulate cloud field sampled on 15 May, the LES model with a double-moment warm-rain microphysics was setup based on available observations and trial and error test simulations. The simulation reproduces the stratocumulus-over-cumulus cloud formations and contrasting macro- and microphysical characteristics of the two cloud layers. The LES model used in this study also includes the delay of cloud water evaporation resulting from the turbulent stirring (Grabowski, 2007; Jarecka et al., 2009) and is capable of predicting homogeneity of the subgrid-scale mixing between the cloud and its cloud-free environment (JGMP13). The homogeneity of the subgrid-scale mixing within the microphysics scheme is controlled by a single parameter α, with the range of values between 0 to 1. The limiting values represent the homogeneous and the extremely inhomogeneous mixing scenarios, respectively. The parameter α depends on the characteristic time scales of the droplet evaporation and of the turbulent homogenization. In the model, these scales are derived locally based on the subgrid-scale turbulent kinetic energy, spatial scale of cloudy filaments, the mean cloud droplet radius, and the humidity of the cloud-free air entrained into the cloud. As a result, parameter α is locally predicted. Subgrid-scale mixing turned out to be on average quite inhomogeneous, with the mean parameter α around 0.7 across the entire depth of the cloud field. However, local variations of α at a given height were large and covered almost the entire range, especially near the base and the top of the cloud field. The

ACPD
13, 1489–1526, 2013

uniform mixing characteristics across the entire depth of the cloud field were explained by small changes of the mixing and evaporation time scales between cumulus and stratocumulus layers.

Appendix A

Summary of model formulas determining the homogeneity of mixing

A Homogeneity of the subgrid-scale turbulent mixing in the double-moment microphysics scheme is determined by the parameter α. This parameter is used to calculate the final droplet concentration after entrainment and turbulent mixing according to the Eq. (11) in Morrison and Grabowski (2008), that is:

$$N_c^f = N_c^i \left(\frac{q_c^f}{q_c^i} \right)^{\alpha} , \quad \text{(A1)}$$

where q_c^i and N_c^i are values of the cloud water mixing ratio and droplet concentration before including effects of evaporation due to the subgrid-scale mixing. These values include all other processes, such as the resolved (advective) and parameterized (subgrid-scale) transport and evaporation due to the advective changes of thermodynamic properties, the vertical advection in particular; q_c^f is the final cloud water mixing ratios (i.e. after the microphysical adjustment). Note that, in the Morrison and Grabowski (2008) scheme, the microphysical adjustment of the cloud water mixing ratio q_c takes place before adjusting N_c, and it is dictated by the predicted supersaturation, and characteristics of the cloud droplet population (i.e. the droplet concentration and size). In the model used here, it also depends on the subgrid-scale structure (i.e. scale of cloudy filaments λ and cloudy fraction of the gridbox β) as explained in Sect. 3. Finally, N_c^f is the final droplet concentration after microphysical adjustment due to the subgrid-scale evaporation and it depends on the α value. The parameter α varies from

ACPD
13, 1489–1526, 2013

0 for the case of the homogeneous mixing (i.e. no change to N_c) to 1 for the extremely inhomogeneous mixing (i.e. when N_c changes in the same proportion as q_c and thus the mean volume radius remains unchanged).

To predict the local value of parameter α, we first relate it to the slope δ from the $r^3 - N$ diagram applied in Andrejczuk et al. (2004, 2006). In this diagram, the total number of droplets is plotted against the mean volume radius cubed, similarly to the diagram used in Burnet and Brenguier (2007). The vertical line (reduction of the number of droplets without changing the size; $\delta \to \infty$) implies extremely inhomogeneous mixing. The homogeneous mixing corresponds to the horizontal line (i.e. changing droplet size without changing the number of droplets; $\delta = 0$). The slope δ is related to the parameter α in Eq. (A1) as:

$$\alpha = \frac{\delta}{1+\delta}. \tag{A2}$$

Based on a large set of DNS simulations, δ can be assumed to be approximately equal to the ratio of the time scales of turbulent homogenization and droplet evaporation (see Fig. 2 in Andrejczuk et al., 2009):

$$\delta \approx \frac{\tau_{\mathrm{mix}}}{\tau_{\mathrm{evap}}}, \tag{A3}$$

where τ_{mix} and τ_{evap} are the turbulent mixing and droplet evaporation time scales respectively. The turbulent homogenization time scale, following Andrejczuk et al. (2009), is approximated by the eddy turnover time (e.g. Jensen and Baker, 1989):

$$\tau_{\mathrm{mix}} = \lambda / u(\lambda), \tag{A4}$$

where $u(\lambda)$ is the characteristic velocity at the filament scale λ. It can be related to the model-predicted TKE (E) as $u(\lambda) = (E)^{1/2}(\lambda/\Lambda)^{1/3}$. This relationship assumes the inertial range scaling for subgrid-scale turbulence and considers TKE to be dominated by

ACPD
13, 1489–1526, 2013

eddies of scale Λ (i.e. $u(\Lambda) \approx (E)^{1/2}$). The droplet evaporation time scale is estimated as

$$\tau_{\text{evap}} = \frac{r^2}{A(1 - \text{RH}_d)}, \tag{A5}$$

where r is the mean volume radius of cloud droplets, RH_d is the relative humidity of the cloud-free portion of the gridbox, and $A \approx 10^{-10}\,\text{m}^2\,\text{s}^{-1}$ is the constant in the droplet diffusional growth equation (i.e. $\text{d}r/\text{d}t = AS/r$, where $S = \text{RH} - 1$ is the supersaturation). RH_d can be estimated using the mean (model-predicted) relative humidity of a gridbox RH and assuming that the cloudy part of the gridbox is saturated. These assumptions lead to

$$\text{RH}_d = \frac{\text{RH} - \beta}{1 - \beta}. \tag{A6}$$

Acknowledgements. EUCAARI-IMPACT data were provided by CNRM Meteo-France (Fred Burnet, Bruno Piguet and Vincent Puygrenier). DJ would like to thank Joanna Slawinska for her assistance with the EULAG model, Hugh Morrison for his assistance with the double-moment microphysics scheme and Sylwester Arabas for his assistance with the experimental data. DJ and HP was partially supported by the European Union 6 FP IP EUCAARI (European Integrated Project on Aerosol Cloud Climate and Air Quality Interactions) No. 036833-2 and the Polish MNiSW grant 396/6/PR UE/2007/7. DJ was additionally supported by the Polish MNiSW grant N N307 128038. DJ and WWG were also partially supported by the NOAA grant NA08OAR4310543, DOE ARM grant DE-FG02-08ER64574, and the NSF Science and Technology Center for Multiscale Modeling of Atmospheric Processes (CMMAP), managed by Colorado State University under cooperative agreement ATM-0425247. AW work was supported by NSF-OCI grants 0904599 and 0904449. Computer time at NCAR was provided by NSF MRI Grants CNS-0421498, CNS-0420873, and CNS-0420985, NSF sponsorship of the National Center for Atmospheric Research, the University of Colorado, and a grant from the IBM Shared University Research (SUR) program. National Center for Atmospheric Research is sponsored by the National Science Foundation.

ACPD
13, 1489–1526, 2013

References

Andrejczuk, M., Grabowski, W. W., Malinowski, S. P., and Smolarkiewicz, P. K.: Numerical simulation of cloud–clear air interfacial mixing, J. Atmos. Sci., 61, 1726–1739, doi:10.1175/1520-0469(2004)061<1726:NSOCAI>2.0.CO;2, 2004. 1505

Andrejczuk, M., Grabowski, W. W., Malinowski, S. P., and Smolarkiewicz, P. K.: Numerical simulation of cloud–clear air interfacial mixing: effects on cloud microphysics, J. Atmos. Sci., 63, 3204–3225, doi:10.1175/JAS3813.1, 2006. 1505

Andrejczuk, M., Grabowski, W. W., Malinowski, S. P., and Smolarkiewicz, P. K.: Numerical simulation of cloud–clear air interfacial mixing: homogeneous versus inhomogeneous mixing, J. Atmos. Sci., 66, 2493–2500, doi:10.1175/2009JAS2956.1, 2009. 1492, 1496, 1505

Baker, M. B. and Latham, J.: The evolution of droplet spectra and the rate of production of embryonic raindrops in small cumulus clouds, J. Atmos. Sci., 36, 1612–1615, 1979. 1492

Baker, M. B., Corbin, R. G., and Latham, J.: The influence of entrainment on the evolution of cloud droplet spectra: I. A model of inhomogeneous mixing, Q. J. Roy. Meteor. Soc., 106, 581–598, doi:10.1002/qj.49710644914, 1980. 1492

Brenguier, J.-L., Bourrianne, T., Coelho, A. A., Isbert, J., Peytavi, R., Trevarin, D., and Weschler, P.: Improvements of droplet size distribution measurements with the Fast-FSSP (Forward Scattering Spectrometer Probe), J. Atmos. Ocean. Tech., 15, 1077–1090, doi:10.1175/1520-0426(1998)015<1077:IODSDM>2.0.CO;2, 1998. 1494

Bretherton, C. S. and Pincus, R.: Cloudiness and marine boundary layer dynamics in the ASTEX Lagrangian experiments. Part I: Synoptic setting and vertical structure, J. Atmos. Sci., 52, 2707–2723, doi:10.1175/1520-0469(1995)052<2707:CAMBLD>2.0.CO;2, 1995. 1494, 1498

Burnet, F. and Brenguier, J.-L.: Observational study of the entrainment-mixing process in warm convective clouds, J. Atmos. Sci., 64, 1995–2011, 2007. 1492, 1501, 1505

Crumeyrolle, S., Weigel, R., Sellegri, K., Roberts, G., Gomes, L., Stohl, A., Laj, P., Bourianne, T., Etcheberry, J. M., Villani, P., Pichon, J. M., and Schwarzenboeck, A.: Impact of cloud processes on aerosol particle properties: results from two ATR-42 flights in an extended stratocumulus cloud layer during the EUCAARI campaign (2008), Atmos. Chem. Phys. Discuss., 11, 33229–33271, doi:10.5194/acpd-11-33229-2011, 2011. 1495

ACPD
13, 1489–1526, 2013

de Roode, S. R. and Duynkerke, P. G.: Observed Lagrangian transition of stratocumulus into cumulus during ASTEX: mean state and turbulence structure, J. Atmos. Sci., 54, 2157–2173, 1997. 1494, 1498

Grabowski, W. W.: Cumulus entrainment, fine-scale mixing, and buoyancy reversal, Q. J. Roy. Meteor. Soc., 119, 935–956, doi:10.1002/qj.49711951305, 1993. 1491

Grabowski, W. W.: Entrainment and mixing in buoyancy-reversing convection with applications to cloud-top entrainment instability, Q. J. Roy. Meteor. Soc., 121, 231–253, doi:10.1002/qj.49712152202, 1995. 1491

Grabowski, W. W.: Representation of turbulent mixing and buoyancy reversal in bulk cloud models, J. Atmos. Sci., 64, 3666–3680, doi:10.1175/JAS4047.1, 2007. 1492, 1495, 1496, 1503

Grabowski, W. W. and Clark, T. L.: Cloud-environment interface instability, rising thermal calculations in two spatial dimensions, J. Atmos. Sci., 48, 527–546, doi:10.1175/1520-0469(1991)048<0527:CIIRTC>2.0.CO;2, 1991. 1491

Grabowski, W. W. and Clark, T. L.: Cloud-environment interface instability, Part II: Extension to three spatial dimensions, J. Atmos. Sci., 50, 555–573, doi:10.1175/1520-0469(1993)050<0555:CEIIPI>2.0.CO;2, 1993a. 1491

Grabowski, W. W. and Clark, T. L.: Cloud-environment interface instability, Part III: Direct influence of environmental shear, J. Atmos. Sci., 50, 3821–3828, doi:10.1175/1520-0469(1993)050<3821:CEIIPI>2.0.CO;2, 1993b. 1491

Grabowski, W. W. and Smolarkiewicz, P. K.: Two-time-level semi-Lagrangian modeling of precipitating clouds, Mon. Weather Rev., 124, 487–497, doi:10.1175/1520-0493(1996)124<0487:TTLSLM>2.0.CO;2, 1996. 1495

Jarecka, D., Grabowski, W. W., and Pawlowska, H.: Modeling of subgrid-scale mixing in large-eddy simulation of shallow convection, J. Atmos. Sci., 66, 2125–2133, doi:10.1175/2009JAS2929.1, 2009. 1492, 1495, 1503

Jarecka, D., Grabowski, W. W., and Pawlowska, H.: Homogeneity of the subgrid-scale turbulent mixing in large-eddy simulation of shallow convection, J. Atmos. Sci., in review, 2013. 1492

Jensen, J. B. and Baker, M. B.: A simple model of droplet spectral evolution during turbulent mixing, J. Atmos. Sci., 46, 2812–2829, doi:10.1175/1520-0469(1989)046<2812:ASMODS>2.0.CO;2, 1989. 1492, 1505

Khairoutdinov, M. and Kogan, Y.: A new cloud physics parameterization in a large-eddy simulation model of marine stratocumulus, Mon. Weather Rev., 128, 229–243, 2000. 1495

ACPD

13, 1489–1526, 2013

Khvorostyanov, V. I. and Curry, J. A.: Aerosol size spectra and CCN activity spectra: reconciling the lognormal, algebraic, and power laws, J. Geophys. Res., 111, 0148–0227, doi:10.1029/2005JD006532, 2006. 1495

Kulmala, M., Asmi, A., Lappalainen, H. K., Baltensperger, U., Brenguier, J.-L., Facchini, M. C., Hansson, H.-C., Hov, Ø., O'Dowd, C. D., Pöschl, U., Wiedensohler, A., Boers, R., Boucher, O., de Leeuw, G., Denier van der Gon, H. A. C., Feichter, J., Krejci, R., Laj, P., Lihavainen, H., Lohmann, U., McFiggans, G., Mentel, T., Pilinis, C., Riipinen, I., Schulz, M., Stohl, A., Swietlicki, E., Vignati, E., Alves, C., Amann, M., Ammann, M., Arabas, S., Artaxo, P., Baars, H., Beddows, D. C. S., Bergström, R., Beukes, J. P., Bilde, M., Burkhart, J. F., Canonaco, F., Clegg, S. L., Coe, H., Crumeyrolle, S., D'Anna, B., Decesari, S., Gilardoni, S., Fischer, M., Fjaeraa, A. M., Fountoukis, C., George, C., Gomes, L., Halloran, P., Hamburger, T., Harrison, R. M., Herrmann, H., Hoffmann, T., Hoose, C., Hu, M., Hyvärinen, A., Hõrrak, U., Iinuma, Y., Iversen, T., Josipovic, M., Kanakidou, M., Kiendler-Scharr, A., Kirkevåg, A., Kiss, G., Klimont, Z., Kolmonen, P., Komppula, M., Kristjánsson, J.-E., Laakso, L., Laaksonen, A., Labonnote, L., Lanz, V. A., Lehtinen, K. E. J., Rizzo, L. V., Makkonen, R., Manninen, H. E., McMeeking, G., Merikanto, J., Minikin, A., Mirme, S., Morgan, W. T., Nemitz, E., O'Donnell, D., Panwar, T. S., Pawlowska, H., Petzold, A., Pienaar, J. J., Pio, C., Plass-Duelmer, C., Prévôt, A. S. H., Pryor, S., Reddington, C. L., Roberts, G., Rosenfeld, D., Schwarz, J., Seland, Ø., Sellegri, K., Shen, X. J., Shiraiwa, M., Siebert, H., Sierau, B., Simpson, D., Sun, J. Y., Topping, D., Tunved, P., Vaattovaara, P., Vakkari, V., Veefkind, J. P., Visschedijk, A., Vuollekoski, H., Vuolo, R., Wehner, B., Wildt, J., Woodward, S., Worsnop, D. R., van Zadelhoff, G.-J., Zardini, A. A., Zhang, K., van Zyl, P. G., Kerminen, V.-M., S Carslaw, K., and Pandis, S. N.: General overview: European Integrated project on Aerosol Cloud Climate and Air Quality interactions (EUCAARI) – integrating aerosol research from nano to global scales, Atmos. Chem. Phys., 11, 13061–13143, doi:10.5194/acp-11-13061-2011, 2011. 1493

Kuo, H.-C. and Schubert, W. H.: Stability of cloud-topped boundary layers, Q. J. Roy. Meteor. Soc., 114, 887–916, doi:10.1002/qj.49711448204, 1988. 1491

Kurowski, M., Malinowski, S. P., and Grabowski, W. W.: A numerical investigation of entrainment and transport within a stratocumulus-topped boundary layer, Q. J. Roy. Meteor. Soc., 135, 77–92, doi:10.1002/qj.354, 2009. 1500

ACPD
13, 1489–1526, 2013

Lehmann, K., Siebert, H., and Shaw, R. A.: Homogeneous and inhomogeneous mixing in cumulus clouds: dependence on local turbulence structure, J. Atmos. Sci., 66, 3641–3659, 2009. 1492

Margolin, L. G., Smolarkiewicz, P. K., and Sorbjan, Z.: Large-eddy simulations of convective boundary layers using nonoscillatory differencing, Physica D, 133, 390–397, doi:10.1016/S0167-2789(99)00083-4, 1999. 1495

Morrison, H. and Grabowski, W. W.: Comparison of bulk and bin warm-rain microphysics models using a kinematic framework, J. Atmos. Sci., 64, 2839–2861, doi:10.1175/JAS3980, 2007. 1495, 1496

Morrison, H. and Grabowski, W. W.: Modeling supersaturation and subgrid-scale mixing with two-moment bulk warm microphysics, J. Atmos. Sci., 65, 792–812, doi:10.1175/2007JAS2374.1, 2008. 1495, 1496, 1504

Prusa, J. M., Smolarkiewicz, P. K., and Wyszogrodzki, A. A.: EULAG, a computational model for multiscale flows, Comput. Fluids, 37, 1193–1207, doi:10.1016/j.compfluid.2007.12.001, 2008. 1495

Puygrenier, V., Brenguier, J.-L., Burnet, F., Gomes, L., and Thouron, O.: LES simulation of a stratocumulus diurnal cycle, in: Proceedings of 2009 EUCAARI Annual Meeting, 275–278, 2010. 1493

Sandu, I., Stevens, B., and Pincus, R.: On the transitions in marine boundary layer cloudiness, Atmos. Chem. Phys., 10, 2377–2391, doi:10.5194/acp-10-2377-2010, 2010. 1494, 1498

Siebesma, A. P., Bretherton, C. S., Brown, A., Chlond, A., Cuxart, J., Duynkerke, P. G., Jiang, H., Khairoutdinov, M., Lewellen, D., Moeng, C.-H., Sanchez, E., Stevens, B., and Stevens, D. E.: A large eddy simulation intercomparison study of shallow cumulus convection, J. Atmos. Sci., 60, 1201–1219, doi:10.1175/1520-0469(2003)60<1201:ALESIS>2.0.CO;2, 2003. 1497, 1501

Siems, S. T., Bretherton, C. S., Baker, M. B., Shy, S., and Breidenthal, R. E.: Buoyancy reversal and cloud-top entrainment instability, Q. J. Roy. Meteor. Soc., 116, 705–739, doi:10.1002/qj.49711649309, 1990. 1491

Smolarkiewicz, P. K. and Margolin, L. G.: Onforward-in-time differencing for fluids: An Eulerian/semi-Lagrangian nonhydrostatic model for stratified flows, Atmos. Ocean Special, 35, 127–152, 1997. 1495

Stevens, B., Moeng, C.-H., Ackerman, A. S., Bretherton, C. S., Chlond, A., de Roode, S., Edwards, J., Golaz, J.-C., Jiang, H., Khairoutdinov, M., Kirkpatrick, M. P., Lewellen, D. C.,

ACPD
13, 1489–1526, 2013

Lock, A., Müller, F., Stevens, D. E., Whelan, E., and Zhu, P.: Evaluation of large-eddy simulations via observations of nocturnal marine stratocumulus, Mon. Weather Review, 133, 1443–1462, 2005. 1497, 1498, 1501

ACPD
13, 1489–1526, 2013

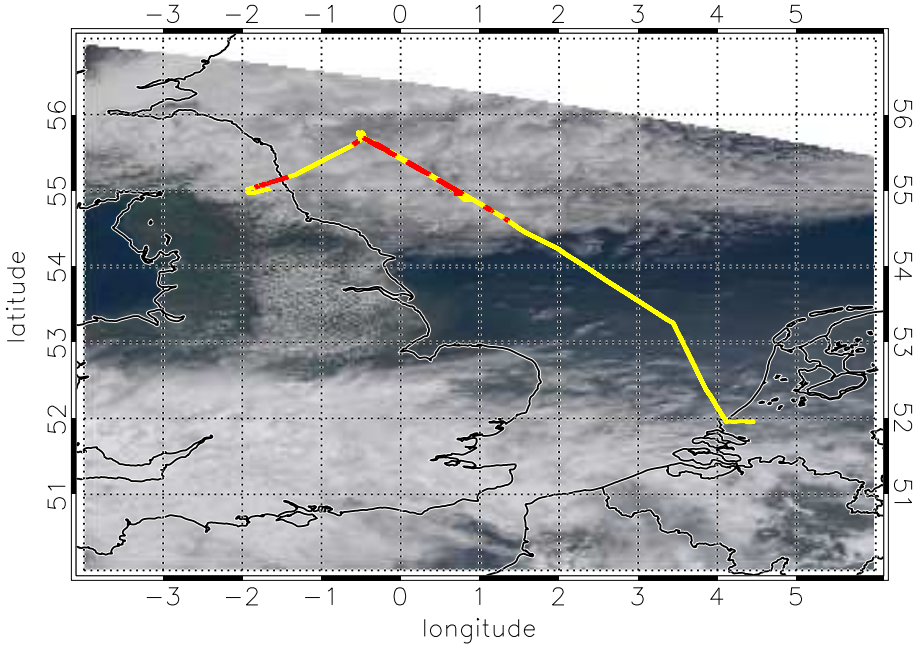

Fig. 1. Image from the Moderate Resolution Imaging Spectroradiometer (MODIS) system (Terra satellite, 11:15 UTC). Yellow line shows the trajectory of the ATR-42 morning flight on 15 May. Red sedments indicate periods where aircraft encountered a cloud.

ACPD
13, 1489–1526, 2013

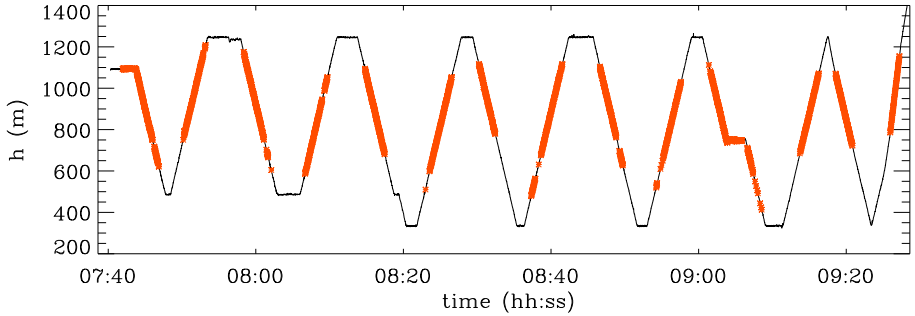

Fig. 2. Height of the aircraft ATR-42 as a function of time. Red color marks periods when aircraft encountered a cloud.

ACPD
13, 1489–1526, 2013

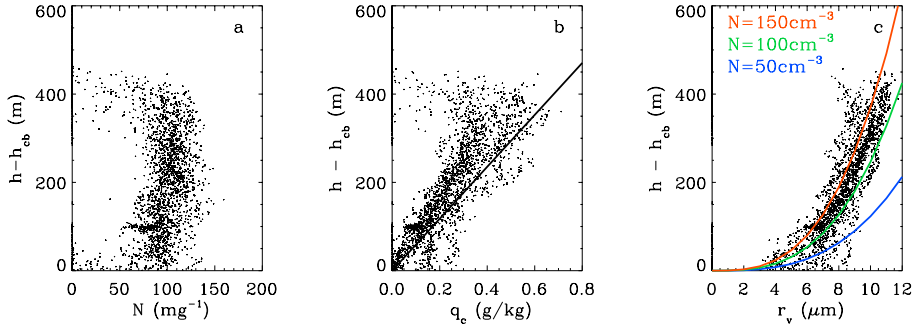

Fig. 3. Experimental data from the stratocumulus cloud layer. **(a)**: cloud droplet concentration; **(b)**: cloud water mixing ratio; **(c)**: mean droplet volume radius. Vertical axes represent height above the cloud base, h_{cb}, estimated separately for each aircraft penetration into the clouds. Color lines in **(c)** mark profiles of the adiabatic droplet radius for different droplet concentration.

ACPD
13, 1489–1526, 2013

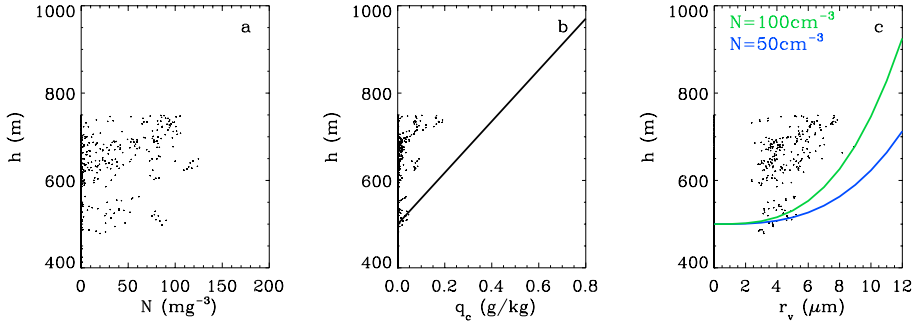

Fig. 4. As Fig. 3, except for the cumulus cloud layer.

ACPD
13, 1489–1526, 2013

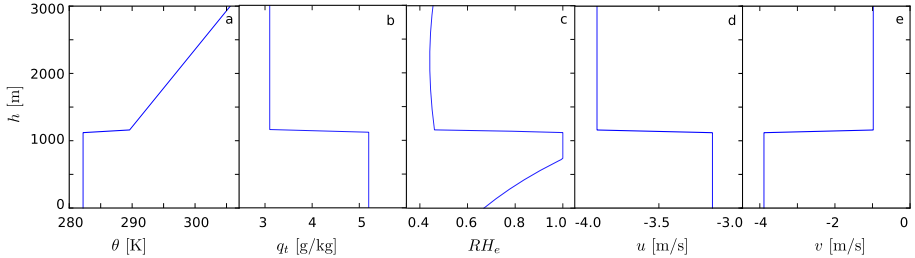

Fig. 5. Idealized profiles of observed mean conditions used to initialize the simulation. **(a)** Potential temperature θ; **(b)** total cloud water mixing ratio q_t; **(c)** relative humidity RH_e; **(d)** zonal wind u; **(e)** meridional wind v.

ACPD
13, 1489–1526, 2013

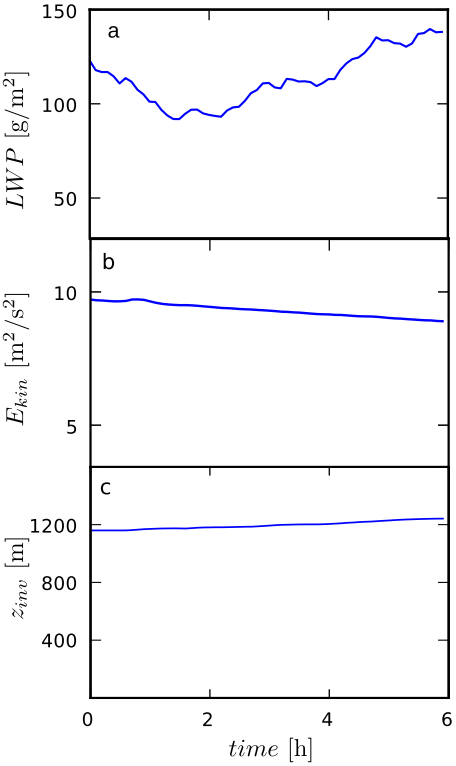

Fig. 6. Evolution of selected bulk properties of the STBL for the entire length of the simulation. **(a)** Liquid water path (LWP), **(b)** resolved kinetic energy per unit of mass, E_{kin}; **(c)** height of the inversion, z_{inv}.

ACPD
13, 1489–1526, 2013

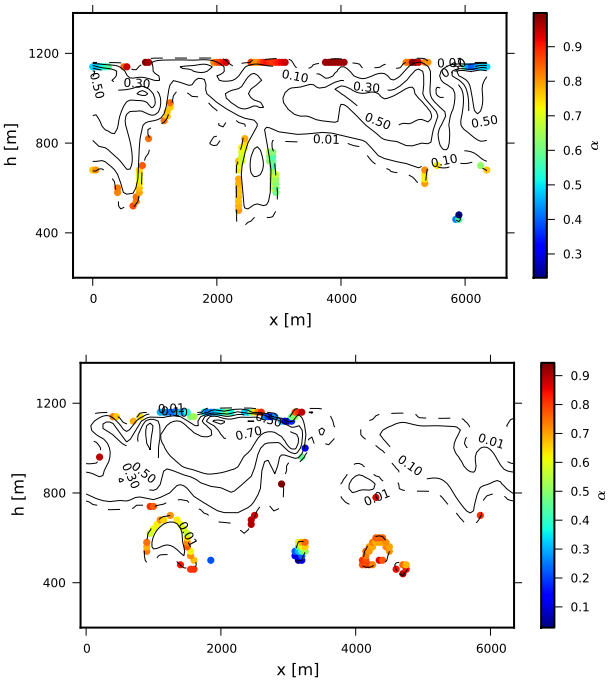

Fig. 7. Snapshots of the cloud water field in two vertical cross sections of the computational domain at time of $t = 6$ h. Colored points show local values of the parameter α at points undergoing turbulent cloud-environment mixing.

ACPD
13, 1489–1526, 2013

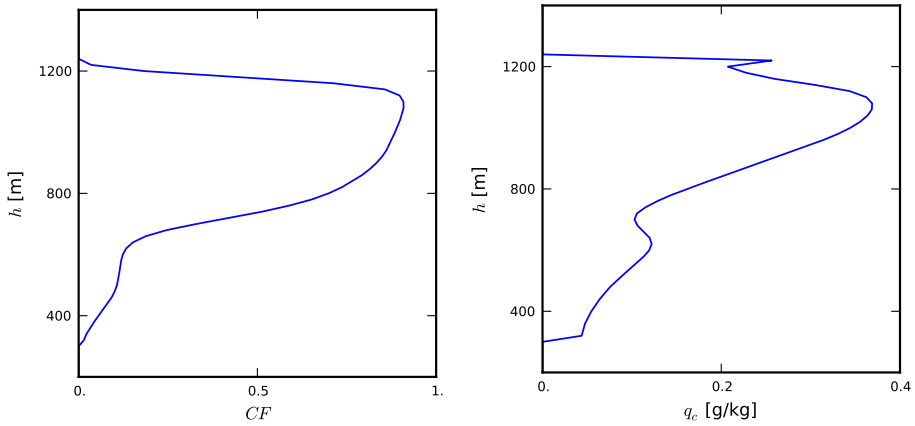

Fig. 8. Average profiles of the cloud fraction, CF, and the cloud water mixing ratio, q_c.

ACPD
13, 1489–1526, 2013

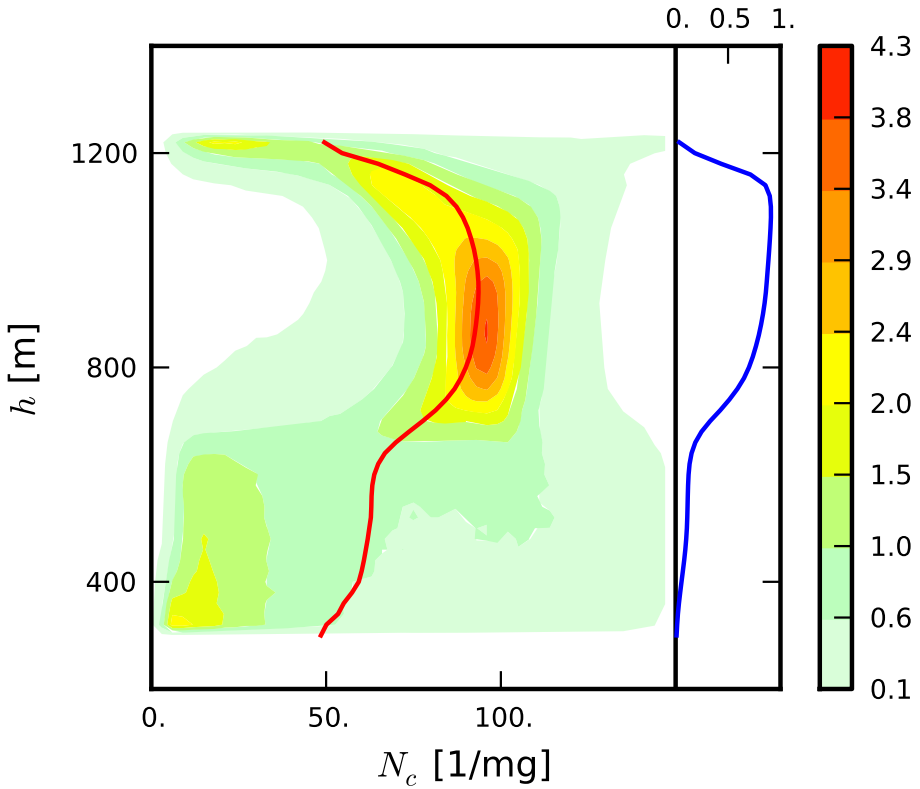

Fig. 9. CFAD of the droplet concentration N_c. Red line shows the average profile. Only cloudy points are included; the cloud fraction profile is shown on the right hand side of the panel with a blue line.

ACPD
13, 1489–1526, 2013

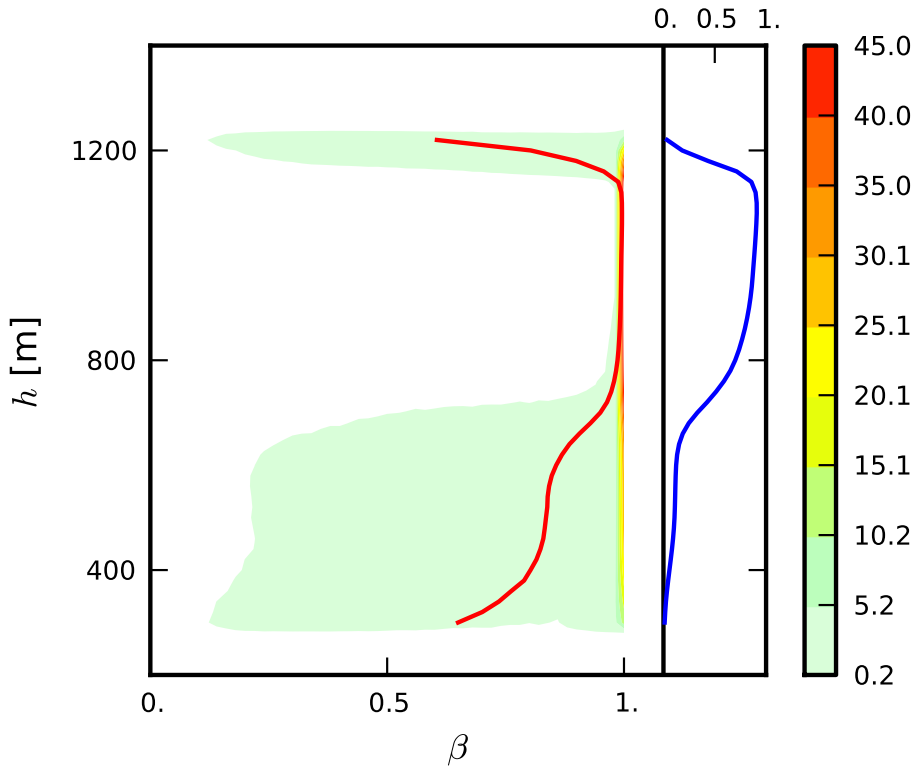

Fig. 10. CFAD of the fraction of a gridbox occupied by the cloudy air β. Red line shows the average profile. Only cloudy points are included; the cloud fraction profile is shown on the right hand side of the panel with a blue line.

ACPD
13, 1489–1526, 2013

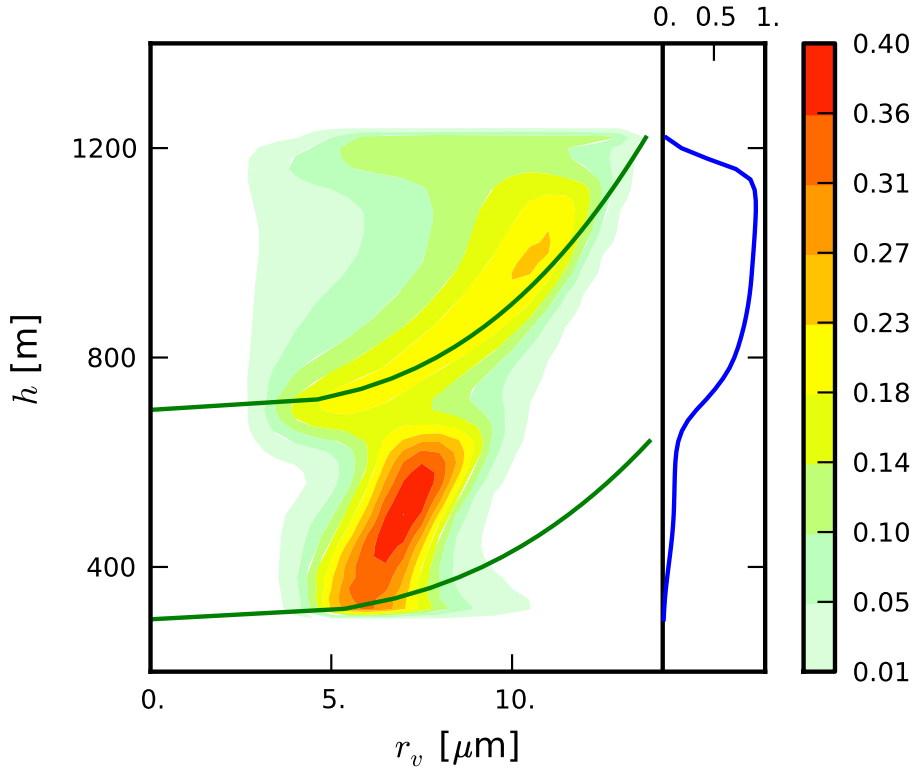

Fig. 11. CFAD of the droplet mean volume radius r_v. Green lines show the adiabatic values of the radius assuming the cloud base height and the adiabatic droplet concentration of 300 m and 60 mg^{-1} for the cumulus layer, and 700 m and 90 mg^{-1} for the stratocumulus layer. Only cloudy points are included; the cloud fraction profile is shown on the right hand side of the panel with a blue line.

ACPD
13, 1489–1526, 2013

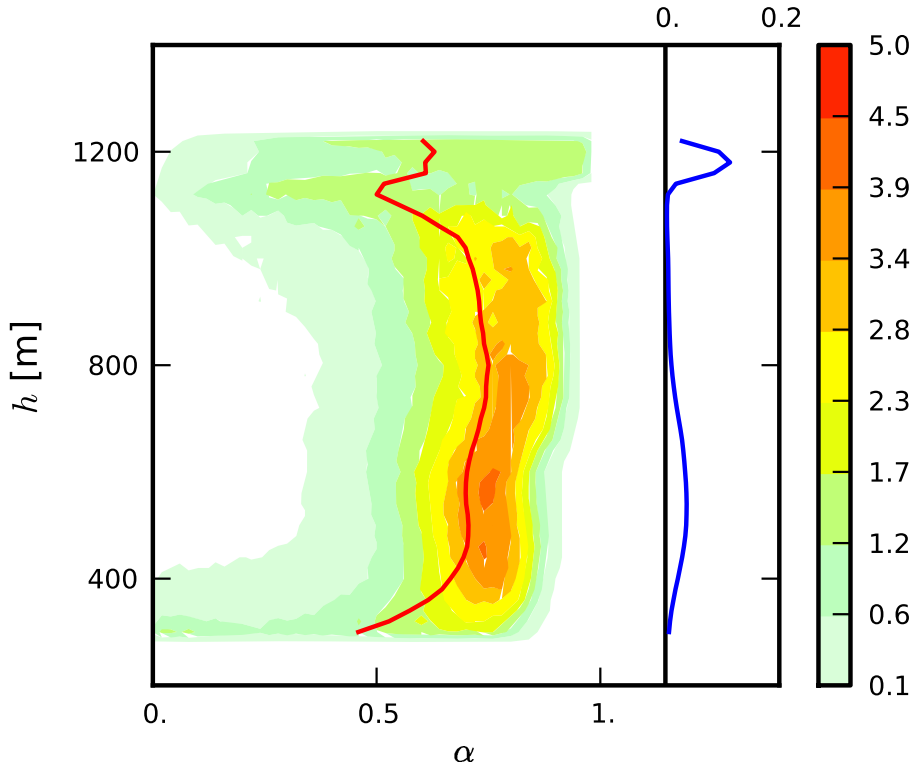

Fig. 12. CFAD of the α parameter. Red line shows the average profile. Only cloudy points where subgrid-scale mixing takes place are included. The frequency of mixing events (i.e. the number of points undergoing turbulent mixing divided by total number of points at each level) is shown on the right hand side of the panel with a blue line.

ACPD
13, 1489–1526, 2013

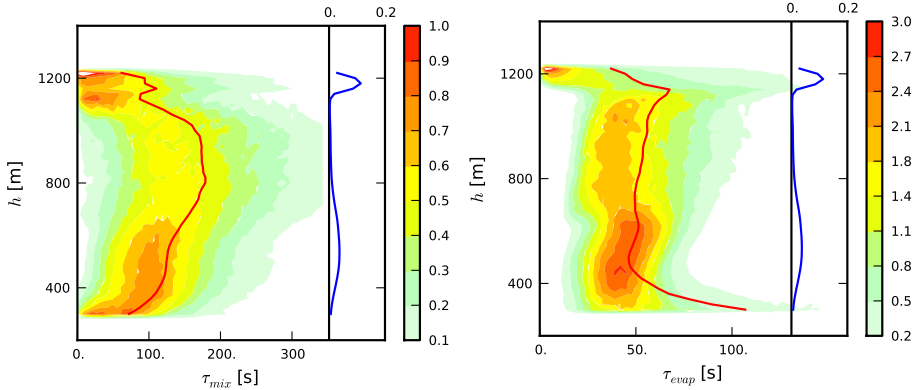

Fig. 13. CFADs of the mixing time scale τ_{mix} and the evaporation time scale τ_{evap}. Red lines show the average profiles. As in Fig. 12, only cloudy points where subgrid-scale mixing takes place are included; the frequencies of mixing events are shown on the right hand sides of the panels.

ACPD
13, 1489–1526, 2013

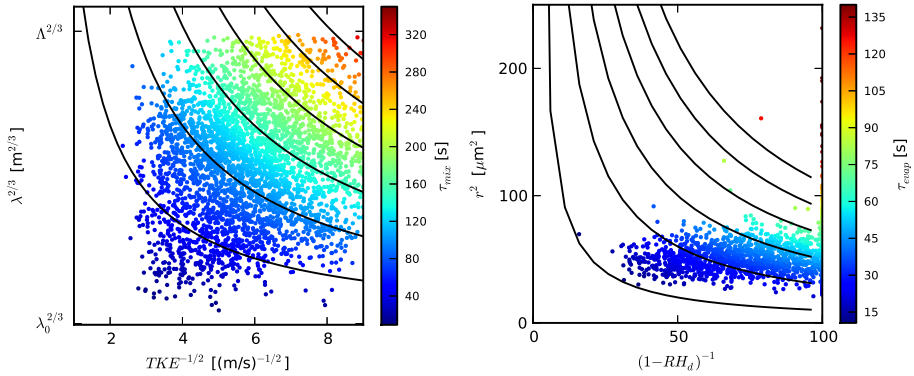

Fig. 14. Scatter plots of model variables (in appropriate powers, see the Appendix A) that determine the actual values of the τ_{mix} and τ_{evap} at the height of 500 m (i.e. within the cumulus layer). Color scales correspond to the time scales values and black lines represent isolines of the time scales.

ACPD
13, 1489–1526, 2013

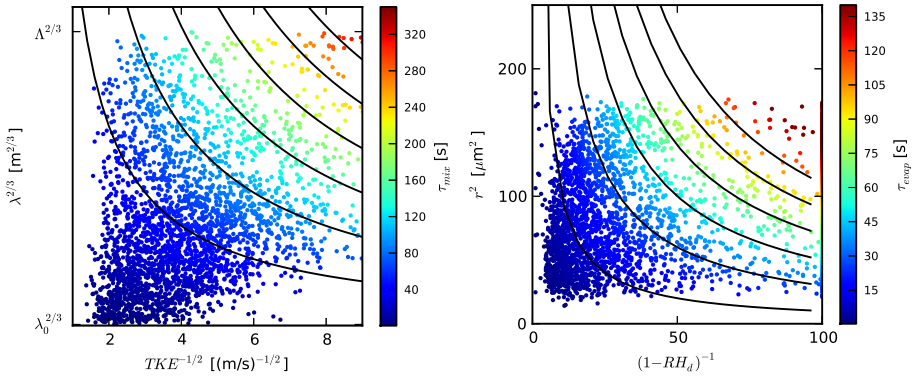

Fig. 15. As Fig. 14, but at the height of 1200 m (i.e. neat the top of the stratocumulus layer).

ACPD
13, 1489–1526, 2013